Infrared interferometry for rough surface measurements: application to failure characterization and flaw detection

Jaydeep K. Sinha
Hareesh V. Tippur
Auburn University
Department of Mechanical Engineering
202 Ross Hall
Auburn, Alabama 36849-5341
E-mail: htippur@eng.auburn.edu

Abstract. A real-time, full-field, noncontacting infrared Twyman-Green interferometer for performing deformation measurements has been developed. The choice of the wavelength offers the advantage of using the interferometer with structural components with little or no surface preparation. The limitation on the surface roughness/texture commonly encountered when using visible light is circumvented through a favorable roughness-to-wavelength ratio. Planar objects with a surface roughness up to $\sigma_a \approx 1$ μm (or surfaces prepared using fixed abrasives with mean grit sizes up to 250 μm) have been examined. Capability of the interferometer for quantifying deformations when dealing with rough surface measurements is demonstrated. Examples of defect detection as well as elastoplastic crack-tip-field mapping are provided. [S0091-3286(97)03908-1]

Subject terms: infrared interferometers; Twyman-Green interferometers; rough surface measurements; crack tip fields; flaw detection.

Paper 13017 received Jan. 10, 1997; accepted for publication Apr. 10, 1997.

1 Introduction

Optical techniques capable of providing full-field, real-time measurements without resorting to elaborate preparation of the material surfaces under investigation, preferably with little or no surface preparation, would have a great deal of practical significance. A potential method for dealing with surfaces in as-is condition for real-time interferometric purposes is based on the results on the scattering of light by rough surfaces due to Beckmann and Spizzichino.[1] Their analysis shows that the specular component of the scattered field increases with increasing wavelength for a randomly rough surface. Munnerlyn and Latta[2] used mid-infrared radiation to relate fringe contrast and surface roughness by measuring the average intensity of an optical component. Some investigations have constructed interferometric setups using coherent infrared radiation. Optical component testing along with some quantitative insight into the influence of roughness of fringe contrast in the mid-infrared range of 10.6 μm is reported by Kwon et al.[3] Recently, Lewandowski et al.[4] have demonstrated infrared holographic interferometry facilitating fringe interpretations for large object displacements and minimizing the handicaps of visible holography. Persson[5] has performed roughness measurement on machined surfaces using a speckle technique. In this work, it is suggested that the measurement range could be extended if the experiments were performed in the infrared range.

In this paper an infrared Twyman-Green interferometer (wavelength 10.6 μm) has been developed for failure characterization and flaw detection through rough surface measurements. The interferometer has real-time, full-field, and noncontact measurement capabilities. In addition, the limitation on the surface roughness/texture commonly encountered when using visible radiation has been successfully overcome by a favorable roughness-to-wavelength ratio using infrared wavelengths. This offers greater latitude in dealing with material surfaces in as-is conditions to perform real-time measurements, unlike conventional double-exposure schemes used with visible radiation.

2 Optical Setup: Twyman-Green Interferometer

The optical setup for the infrared Twyman-Green interferometer is shown in Fig. 1. It consists of a CO_2 laser, lenses (L_1, L_2, and L_3), beamsplitters (BS1 and BS2), a reference mirror, and a pyroviewer camera connected to a TV monitor and a hard-copy unit. The object to be investigated is a typical rough surface encountered in engineering practice. The optical interference is a result of the path difference between the reference and test paths as shown.

A water-cooled CO_2 laser (Invar-stabilized Synrad E48-I) operating at 10.6-μm wavelength with continuous 7.5-W output power (stability $\pm 2\%$) was used as a coherent light source. The unexpanded laser beam is 3.5 mm in diameter and is vertically polarized. A universal controller (Synrad UC-1000) is used for a general-purpose interface between the user signal and CO_2 laser, adding flexibility of power output control. The experiments reported in this paper have been conducted with low power levels of approximately 5% of the nominal power of the laser. Two ZnSe lenses L_1 and L_2 were used to expand the laser beam to approximately 35-mm diam. All lenses used were of meniscus type to minimize spherical aberrations. A ZnSe (50 : 50) beamsplitter was used to split the beam into two components as shown in Fig. 1. The optical coatings are of dielectric type and are optimized for 10.6-μm wavelength and 45-deg ($\pm 2\%$) incidence. The reference mirror is an aluminum-coated first surface mirror. A Pyroviewer camera

(model 5450, Electrophysics Inc.) is used for imaging the interference fringes. This camera is designed to detect radiation in the 8–14-μm region. The recommended power threshold to prevent damage to the camera detector is 1 mW/cm^2. This being a rather small power, further reduction in the light intensity entering the optical setup is accomplished by a 80 : 20 ZnSe beamsplitter (BS2) as shown in Fig. 1. Fluorescent target plates were used for aligning the optics.

3 Rough Surface Interferometry: Interference Analysis

Often real-time interferometric investigations involving metallic objects require elaborate preparation (creating a specularly reflective surface, printing gratings, etc.) of the surface because the ones encountered in engineering practice are rough and the differences are only in the degree and the type of roughness. Identifying the degree of roughness depends on both the geometry and the wavelength of the incident probe and is taken advantage of in this work. Roughness is generally classified as periodic roughness, as in the case of machined surfaces, and nonperiodic roughness, such as the random roughness of a sandblasted surface. When a surface is illuminated with coherent light, the surface roughness and the orientation of the surface determine the general scattering pattern. As the surface roughness increases, the surface is perceived as changing from smooth or specular to rough or diffuse. That is, the specular component of light decreases and the diffused light component increases with increasing roughness. Thus specular reflection can be used as a measure of surface roughness. The Rayleigh criterion characterizes the smoothness of a surface in terms of a parameter $\varepsilon_R = (4\pi a/\lambda)\cos\theta_i$ ($\ll 1$), where a is the surface peak amplitude, λ is the wavelength of the incident light, and θ_i is the incident angle. Evidently, there are two ways of reducing ε_R ($\ll 1$): (1) by increasing θ_i and thus causing $\cos\theta_i$ to get smaller, and (2) by increasing the wavelength λ of the incident light. Because the wavelength increase can be over an order of magnitude from the mid-visible to the mid-infrared range and the cosine function decreases as θ_i varies from 0 to 90 deg, it should be possible to extend the measurement techniques to surfaces that are traditionally considered far from being optically smooth.

In this work, the wavelength of light in a Twyman-Green interferometer was increased to perform out-of-plane deformation measurements on machined or natural surfaces. First, a study of the discernability of interference patterns in situations involving different surface roughness to test the feasibility of using ir interferometry was performed. The fringe visibility and fringe contrast data were used to quantify operational limits of this interferometer in dealing with rough surfaces.

In the following analysis of the interferometer, zeroth-order waves are considered for normal incidence of light on the beam object surface. Let l_1, l_2, and l_3 denote geometric path lengths of the interferometer as shown in Fig. 1. The complex amplitudes corresponding to the reference and the test paths can be expressed by

$$E_1 = A_1 \exp[ik(2l_1 + l_3)] \tag{1}$$

$$E_2 = A_2 \exp\{ik[2l_2 + l_3 + 2h(x,y) + 2w(x,y)]\}, \tag{2}$$

where k ($=2\pi/\lambda$) is the wave number and $h(x,y)$ is the local surface height measured relative to the zero mean (see insert in Fig. 1). Also, in Eq. (2), $w(x,y)$ represent out-of-plane deformation of the mean surface of the object. Then, the intensity distribution

$$\begin{aligned} I &= (E_1 + E_2)(E_1 + E_2)^* \\ &= A_1^2 + A_2^2 + 2A_1A_2 \cos(k\{2[(l_1 - l_2) - w(x,y)] \\ &\quad - 2h(x,y)\}), \end{aligned} \tag{3}$$

where $(\cdot)^*$ denotes the complex conjugate. The roughness of the surface influences the contrast of the fringes. In order to quantify contrast while dealing with random rough surfaces such as the ones in this work, we assume a Gaussian probability density function of the surface height distribution.[6] A Gaussian surface height distribution with standard deviation σ has a probability distribution function

$$p(h) = \frac{1}{\sigma(2\pi)^{1/2}} \exp\left(\frac{-h^2}{2\sigma^2}\right). \tag{4}$$

Then the ensemble average of the phase variability $\Delta\phi$ due to roughness is given by

$$\langle \exp(i\Delta\varphi) \rangle = \int_{-\infty}^{+\infty} \exp(2ikh)\ p(h)\ \mathrm{d}h. \tag{5}$$

Integrating Eq. (5) after separating the real and imaginary terms, we get

$$\cos[2kh(x,y)] = \exp(-2k^2\sigma^2), \quad \sin[2kh(x,y)] = 0. \tag{6}$$

By expanding the cosine term in Eq. (3) and substituting Eq. (6), the expression for intensity simplifies to

$$\begin{aligned} I(x,y) &= A_1^2 + A_2^2 + 2A_1A_2 \exp(-2k^2\sigma^2)\cos\{2k[(l_1 - l_2) \\ &\quad - w(x,y)]\}. \end{aligned} \tag{7}$$

From the above, the fringe contrast C can be obtained as

$$C = \frac{I_{\max} - I_{\min}}{I_{\max} + I_{\min}} = C_a C_\sigma, \tag{8}$$

where

$$C_a = \frac{2A_1A_2}{A_1^2 + A_2^2} \quad \text{and} \quad C_\sigma = \exp\left(\frac{-8\pi^2\sigma^2}{\lambda^2}\right).$$

In the above, C_a is due to maximum amplitudes in the reference and test paths of the optical setup, while C_σ is due to surface roughness. For simplicity, let us assume $l_1 = l_2 = l$. Then for constructive interference, the argument of the cosine term in Eq. (7) should be equal to $2N\pi$, where N is an integer. This leads to

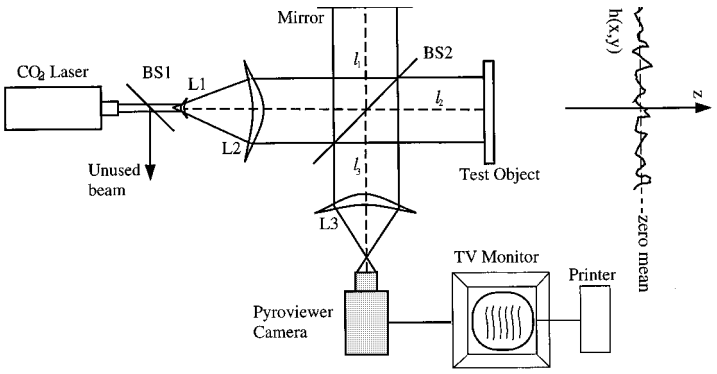

Fig. 1 Infrared Twyman-Green interferometer for rough surface measurements.

$$w(x,y)=\frac{N\lambda}{2}, \tag{9}$$

where $N = 0, \pm 1, \pm 2, \ldots$ represent fringe orders. Thus the light fringe occurs for every $\lambda/2$ change in the path length, and one could readily obtain a sensitivity of $\lambda/4$ ($=2.5\ \mu$m) by utilizing both dark and light fringes.

4 Experiments

4.1 *Surface Roughness and Fringe Contrast*

First, experiments to determine the ability of the interferometer to deal with various degrees of random roughness were carried out. A sample was made of an aluminum blank and was manually polished using different fixed abrasives to produce different roughness variations. This method also represents the most common method of preparing surfaces for measurement purposes. The roughness of the prepared surface was measured using a surface profilometer to obtain the arithmetic-average roughness σ_a. The measurements reported here represent a mean value of multiple measurements. The measurements were converted into root-mean-square values[7] σ for subsequent analysis. The sample with different surface roughness was studied under the same experimental conditions. Different fixed abrasive sheets (emery paper, from #2000 with mean grit size 1 μm to #60 with mean grit size 250 μm) were used under dry conditions to alter the surface roughness of the sample between experiments. The interferometric fringes were scanned to obtain bitmap files, and the intensity profiles were plotted using Matlab. Some examples are shown in Fig. 2. These intensity profiles were subsequently analyzed to quantify the fringe contrast. Plots of the normalized (with respect to a mirrorlike surface) fringe contrast as a function of the surface roughness parameter and of the grit size are shown in Fig. 3(a) and Fig. 3(b), respectively. Evidently, as the roughness of the surface increases, the contrast of the fringes deteriorates, as one would expect. The surface quality after polishing with #240 emery paper (mean abrasive grit size 20 μm) was found good enough to obtain reasonable fringe contrast. In many of the experiments reported in this work either #400 and #600 fixed abrasive papers were used.

To demonstrate the flexibility offered by the infrared interferometers, experiments were also performed for a machined surface (surface roughness 0.36 μm in the rolling direction and 0.34 μm in the transverse direction) and a surface spray-painted with commercially available chrome paint. The fringes obtained from these experiments are shown in Fig. 4. Again, good-contrast fringes (fringe contrast $\approx$0.90 for a machined surface and $\approx$0.80 for a painted surface) having excellent discernability were obtained, which suggests the ease of surface preparation for full-field measurement purposes in the proposed scheme.

4.2 *Deformation Measurement: Calibration*

To demonstrate the applicability of this technique for quantitative deformation measurements, a widely studied problem of a laterally loaded circular plate was considered. An aluminum plate (diameter 25 mm, thickness 0.5 mm) with clamped support was subjected to a uniform pressure [Fig. 5(a)], and the out-of-plane displacement contours were mapped in real time. The surface of the plate was machined and prepared using #600 emery paper. The interference patterns from the experiment are shown in Fig. 5(b) for an applied pressure of 15 psi. The measurement sensitivity is 2.5 μm per half fringe.

The out-of-plane displacement w of an elastically deformed circular plate with clamped edge boundary conditions is given by[8]

$$w(r)=\frac{p_0}{64D}(R^2-r^2)^2, \tag{10}$$

where p_0 is the applied pressure, $D\ [=Et^3/12(1-\nu^2)]$ is the rigidity (E is Young's modulus, ν is Poisson's ratio, t is the thickness of the plate), R is the radius of the plate, and r is the polar coordinate as shown in Fig. 5(a). A comparison of the optical measurements and the predictions from Eq. (10) are shown in Fig. 5(c). Good agreement between the two is clearly evident.

4.3 *Mapping Elastoplastic Crack Tip Deformations*

Next, out-of-plane deformation measurement near an elastoplastically deformed crack was carried out to demonstrate the potential of the method for failure characterization. An aluminum 6061-T6 beam sample was machined from a 6.25-mm rolled sheet of aluminum without any surface preparation. The span of the beam L was 100 mm, and its

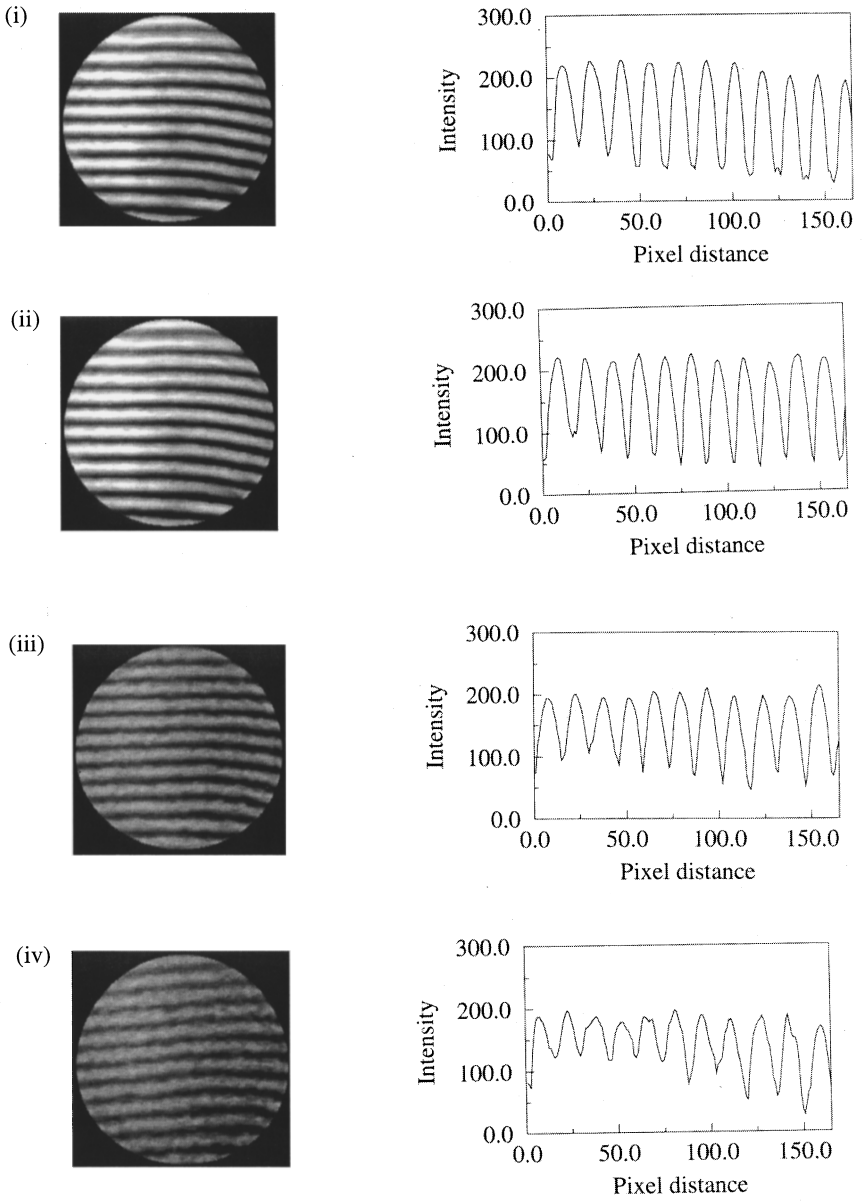

Fig. 2 Typical experimental fringes for aluminum surfaces prepared using different grit size abrasives: (i) #600 (mean grit size of 15 μm), (ii) #400 (20 μm), (iii) #120 (125 μm), (iv) #60 (250 μm). The intensity axis represents gray level, and the horizontal axis represents pixel distance.

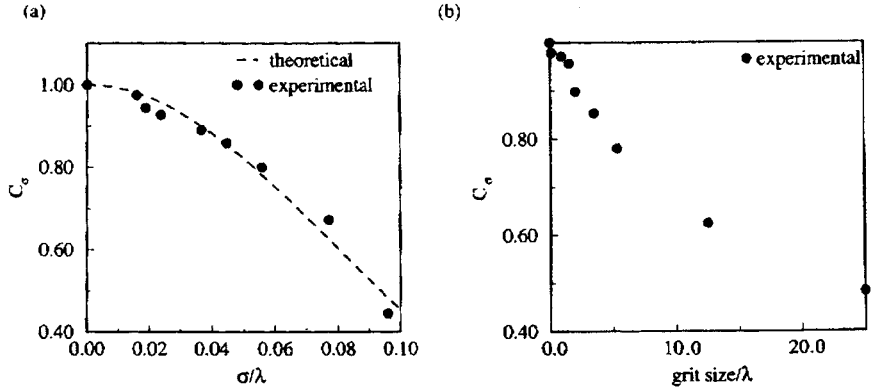

Fig. 3 Plot of fringe contrast as a function of (a) surface roughness (b) grit size.

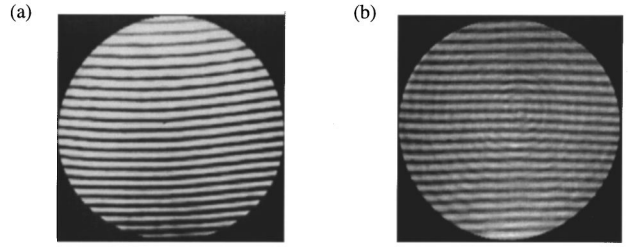

Fig. 4 Typical IR wedge fringe patterns for (a) a machined surface (b) a painted surface.

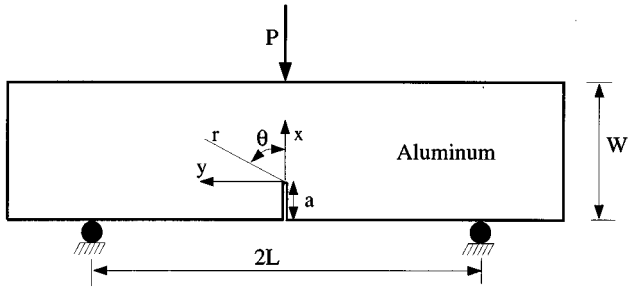

Fig. 6 Three-point bend loading configuration.

width W was 25 mm. A through-the-thickness edge discontinuity of length $a=6$ mm and thickness of approximately 250 μm was machined into the sample using a slitting saw. The specimen and its loading configuration are shown in Fig. 6. The beam was subjected to symmetric three-point bending (mode-I loading). A 0.3-mm-diam pencil lead (of the kind commonly used in mechanical pencils) was temporarily attached to the sample surface to obtain a sharp focus on the crack tip region. A monotonically increasing load was applied to the sample in a displacement-controlled loading device. The crack tip deformations were mapped using the interferometer in real time. Some typical interference patterns representing contours of constant $w(x,y)$ fringes near the crack tip for different load levels are shown in Fig. 7. The average out-of-plane strain ε_z $[\approx 2w(x,y)/B]$ was estimated from these fringes by knowing the nominal thickness B of the beam. From the interference patterns [Fig. 7(b)] the crack tip strain ε_z is approximately 2% and is well beyond the yield strain for aluminum 6061-T6 of approximately 0.4%. The discernability and contrast of the fringes near the crack tip region are very good even in the presence of the extensive plastic deformations. It should be noted that plastic deformation near the crack tip alters the surface texture, which in turn increases the local roughness and affects the fringe contrast when visible light is used. Further, as the crack tip deformation increases, shear lips form on the surface with a large local surface slope [see Fig. 7(c)]. In view of the limited aperture of the optical components, the discernability of the fringes along this shear lip is affected. However, this can be alleviated by using optical components with larger numerical aperture.

The deformations near a ductile crack are predominantly three-dimensional in nature,[9] and full-field 3-D analytical descriptions for them are not available yet. Hence, an elastoplastic, three-dimensional finite-element analysis was carried out using the ANSYS software package. The stress-strain relations necessary for these simulations were obtained from a uniaxial Ramber-Osgood model,

$$\frac{\varepsilon}{\varepsilon_0}=\frac{\sigma}{\sigma_0}+\alpha\left(\frac{\sigma}{\sigma_0}\right)^n, \tag{11}$$

for the beam material from a previous study.[9] In the above, ε_0, σ_0 are the yield strain and stress, n is the material hardening index, and α is a constant. For aluminum 6061-T6, values of $n=18$ and $\alpha=1.22$ were used. Four layers of eight-node (three degrees of freedom per node) brick elements were used in the model, which consisted of 4000 elements and 5226 nodes (see Fig. 8). The model was subjected to three-point bending, as was done in the experiments. The finite-element discretization was fine enough to adequately capture the full-field singular behavior near the crack tip.[10] Next, contours of the out-of-plane displacement $w(x,y)$ were generated from the numerical results on the surface of the model. A direct superposition of the experimental fringes and finite-element contours (broken lines)

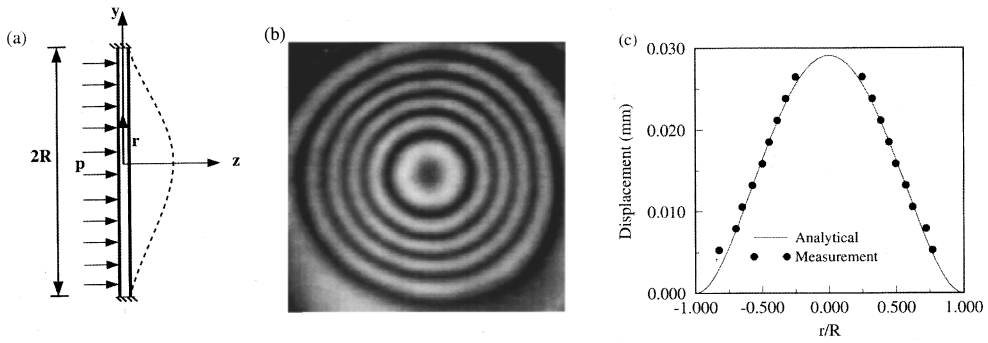

Fig. 5 Calibration experimental results: (a) plate with a clamped support subjected to uniform pressure, (b) out-of-plane displacement (w) contours for a circular blind hole (circular defect) in the plate, (c) comparison of the results with the theoretical predictions.

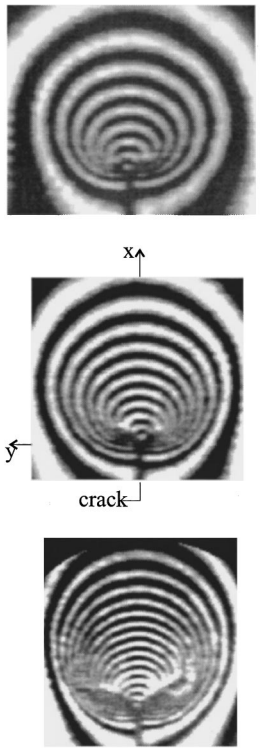

Fig. 7 Selected interference patterns representing contours of $w(x,y)$ fringes near the crack tip for different values of P/P_0: (a) 0.98, (b) 1.04, (c) 1.09.

around the crack tip is shown in Fig. 9. Good agreement between the two results is clearly evident and demonstrates the ability of the interferometer to map deformations in regions of high strain gradients.

4.4 *Subsurface Defect Detection*

To demonstrate the possibility of subsurface flaw detection using the infrared interferometers, experiments with artificially introduced disbonds in a layer bonded to a substrate

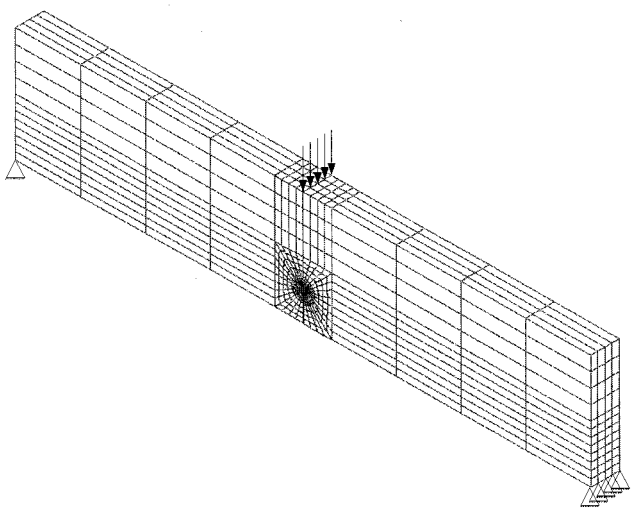

Fig. 8 3-D finite-element mesh used for elastoplastic crack tip simulations.

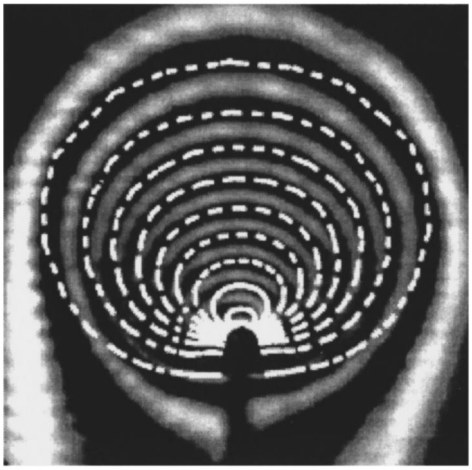

Fig. 9 Superposition of the finite-element contours (broken lines) on the experimentally obtained interferometric fringes, P/P_0:1.04.

were carried out. In these experiments, a 1.25-mm-thick polymeric layer was bonded onto a thick substrate. The polymeric layer was spray-painted with commercially available chrome-aluminum paint to obtain the reflectivity necessary for experimentation. Before bonding the polymeric layer, a circular (≈5-mm diam) and a square (≈5-mm side) Teflon layer approximately 200 μm thick were positioned at two different locations approximately 50 mm apart on the substrate. These inserts introduced local bumps (subsurface defects located at a 1.25-mm depth), which are not evident when the surface is examined visually. However, when scanned in the interferometer, the defects become readily visible, as shown in Fig. 10. The shapes of the two defects become clear from the shapes of the resulting fringe patterns in the neighborhood of the defects. It should be pointed out that ensuring the flatness of the resulting sandwich was not critical, as can be seen by the fringes surrounding the region of defects.

5 Conclusions

An infrared Twyman-Green interferometer has been developed for failure characterization and flaw detection. The ability of the method to perform real-time measurements on rough surfaces is demonstrated. The fringe contrast is reasonably good over the wide range of surface roughness that is encountered in practice or can be produced easily. Satisfactory fringe contrasts (scaled fringe contrast >0.8) have been obtained with surfaces prepared using fixed abrasives

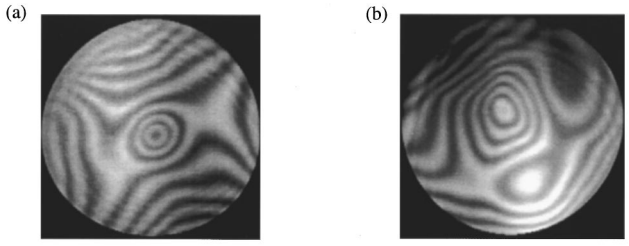

Fig. 10 Subsurface defect detection: (a) circular defect, (b) rectangular defect.

with grit sizes in the range of 1 μm (#2000) to 53 μm (#240). The interferometer was also tested with randomly rough, machined, and spray-painted surfaces to demonstrate the versatility of the interferometer in dealing with field situations. Feasibility of the method for quantifying deformations was demonstrated using a calibration test. The method was next used for investigating out-of-plane crack tip displacements in ductile materials wherein elastoplastic deformations often alter the surface roughness and affect measurements when using visible light. The out-of-plane deformations were compared with a complementary 3-D elastoplastic simulation and the measurements were in good agreement with the computations. The ability of the interferometer to detect subsurface flaws in layered materials with artificially introduced defects is also demonstrated.

References

1. P. Beckmann and A. Spizzichino, *The Scattering of Electromagnetic Waves from Rough Surfaces*, Pergamon, New York (1963).
2. C. R. Munnerlyn and M. Latta, ''Rough surface interferometry using CO_2 laser source,'' *Appl. Opt.* **7**, 1858–1859 (1968).
3. O. Kwon, J. C. Wyant, and C. R. Hayslett, ''Rough surface interferometry at 10.6 μm,'' *Appl. Opt.* **19**, 1862–1869 (1980).
4. J. Lewandowski, ''Lateral shear interferometer for infrared and visible light,'' *Appl. Opt.* **28**, 2373–2379 (1989).
5. U. Persson, ''Roughness measurement of machined surfaces by means of the speckle technique in the visible and infrared regions,'' *Opt. Eng.* **32**, 3327–3332 (1993).
6. B. P. Williamson, J. Pullen, and R. T. Hunt, ''The shape of solid surfaces,'' presented at Surface Mechanics: ASME Winter Annual Meeting, Nov. 16–21, 1969, Los Angeles.
7. J. C. Stover, *Optical Scattering, Measurement and Analysis*, SPIE Optical Engineering Press (1995).
8. S. P. Timoshenko and J. N. Goodier, *Theory of Elasticity*, McGraw-Hill (1970).
9. F. P. Chiang, T. V. Hareesh, B. C. Liu, and S. Li, ''Optical analysis of HRR field,'' *Opt. Eng.* **27**, 625–629 (1988).
10. J. K. Sinha, H. V. Tippur, and L. Xu, ''An interferometric and finite element study of interfacial crack tip fields and the influence of mode-mixity on 3D deformations,'' *Int. J. Solids & Struct.* **34**, 741–754 (1997).

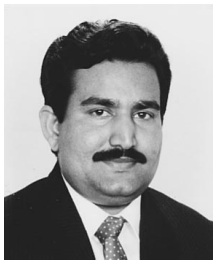

Jaydeep K. Sinha obtained his MSc in physics from Magadh University, India, in 1986 and worked as a research fellow in the laser and spectroscopy lab at Banaras Hindu University, India. He received MS in mechanical engineering from Tuskegee University in 1994. Currently, he is a PhD candidate at Auburn University, conducting research in developing optical techniques and their application to failure characterization and nondestructive testing.

Hareesh V. Tippur obtained MS and PhD degrees from Indian Institute of Science and State University of New York at Stony Brook in 1982 and 1988, respectively. He was a postdoctoral fellow at California Institute of Technology before joining Auburn University in 1990. Currently, he is an associate professor and leads the failure characterization and optical techniques lab at Auburn. He has worked extensively in the area of optical techniques for failure characterization. His work has resulted in combined moiré and laser speckle techniques for simultaneous measurement of all three displacement components near cracks and a new shearing interferometry called *coherent gradient sensing* (CGS) for static and dynamic fracture mechanics studies. He has received the Hetenyi award from the Society of Experimental Mechanics for outstanding research publication in *Experimental Mechanics* and has been recognized as an outstanding new mechanics educator by the American Society for Engineering Education. His current interdisciplinary interests include visible and infrared techniques for metrology, interfacial fracture mechanics, and failure characterization of functionally graded materials.